Molecular mechanisms for the regulation of histone mRNA stem-loop–binding protein by phosphorylation

Jun Zhang[a], Dazhi Tan[b], Eugene F. DeRose[a], Lalith Perera[a], Zbigniew Dominski[c,d], William F. Marzluff[c,d,1], Liang Tong[b,1], and Traci M. Tanaka Hall[a,1]

[a]Laboratory of Structural Biology, National Institute of Environmental Health Sciences, National Institutes of Health, Research Triangle Park, NC 27709; [b]Department of Biological Sciences, Columbia University, New York, NY 10027; [c]Department of Biochemistry and Biophysics and [d]Integrative Program in Biological and Genome Sciences, University of North Carolina, Chapel Hill, NC 27599

Edited by Jennifer A. Doudna, University of California, Berkeley, CA, and approved June 19, 2014 (received for review April 8, 2014)

Replication-dependent histone mRNAs end with a conserved stem loop that is recognized by stem-loop–binding protein (SLBP). The minimal RNA-processing domain of SLBP is phosphorylated at an internal threonine, and *Drosophila* SLBP (dSLBP) also is phosphorylated at four serines in its 18-aa C-terminal tail. We show that phosphorylation of dSLBP increases RNA-binding affinity dramatically, and we use structural and biophysical analyses of dSLBP and a crystal structure of human SLBP phosphorylated on the internal threonine to understand the striking improvement in RNA binding. Together these results suggest that, although the C-terminal tail of dSLBP does not contact the RNA, phosphorylation of the tail promotes SLBP conformations competent for RNA binding and thereby appears to reduce the entropic penalty for the association. Increased negative charge in this C-terminal tail balances positively charged residues, allowing a more compact ensemble of structures in the absence of RNA.

X-ray crystallography | NMR | intrinsically disordered protein

Histone synthesis increases at the beginning of S-phase to package newly replicated DNA with histone proteins, but synthesis must be shut down rapidly and histone mRNA degraded at the end of DNA replication because of the toxicity of surplus histone proteins (1, 2). This cyclic demand for histones requires strict regulation, which is achieved mainly by controlling the synthesis and degradation of histone mRNA (3). Replication-dependent histone mRNAs are the only known cellular mRNAs that are not polyadenylated and instead end with a conserved stem loop (4). Histone mRNAs are generated from longer histone pre-mRNAs as a result of an endonucleolytic cleavage between the stem loop and a purine-rich downstream sequence termed the "histone downstream element" (HDE) (5).

Stem-loop–binding protein (SLBP), also known as "hairpin-binding protein" (6), binds to the histone mRNA stem loop, and U7 small nuclear ribonucleoprotein binds to the HDE (7). Other factors, including the endonuclease CPSF-73, are involved in both polyadenylation and histone mRNA 3′-end processing (8–11). In mammalian nuclear extracts, SLBP is not absolutely required for the biochemical reaction of processing (12). In contrast, cleavage of histone pre-mRNA in *Drosophila* cells and nuclear extracts requires the binding of SLBP to the stem loop (10, 13).

The minimal histone mRNA processing domain of *Drosophila* SLBP contains a 72-aa RNA-binding domain (RBD) unique to SLBPs and an 18-aa C-terminal region (Fig. 1*A*) (14). This RNA-processing domain (RPD) is necessary and sufficient for histone mRNA 3′-end processing in vitro (15). The RBDs of human SLBP (hSLBP) and *Drosophila* SLBP (dSLBP) are phosphorylated at a Thr residue in a conserved TPNK motif (16, 17). The recent crystal structure of hSLBP RBD in complex with histone mRNA stem loop and 3′ hExo, a 3′–5′ exonuclease required for histone mRNA degradation, provided the first molecular insights into the architecture of this complex, and revealed how the hSLBP RBD forms a new RNA-binding motif to interact with the stem-loop RNA (18). On the other hand, how SLBP alone interacts with the RNA or how this interaction might be affected by phosphorylation of the TPNK motif is not known.

The C-terminal region of dSLBP contains a motif, SNSDSDSD, whose hyperphosphorylation is required for efficient processing of histone pre-mRNA (15). Despite the similarity of hSLBP and dSLBP RBDs (55% identical residues) and their ability to bind identical stem-loop RNA sequences, neither SLBP can substitute for the other to process histone pre-mRNA in nuclear extracts; in fact, hSLBP inhibits processing of *Drosophila* histone pre-mRNA (15). This incompatibility results from differences in the C-terminal region (Fig. 1). The sequence C-terminal to the RBD in hSLBP is required for processing, but it is longer, has no similarity to the *Drosophila* sequence, and lacks phosphorylation sites.

Here we focused on dSLBP and showed that phosphorylation greatly increases dSLBP binding affinity for the histone mRNA stem loop. Mimicking phosphorylation of the dSLBP RPD by mutation of phosphorylation sites to Glu residues at both the TPNK motif and the C-terminal region also boosted binding affinity relative to the nonphosphorylated dSLBP RPD. Structural studies of both the human and *Drosophila* SLBP RPD indicated that phosphorylation of the TPNK motif stabilizes the

Significance

As DNA is replicated during cell division, it must be packaged by histones. To match the level of available histones to DNA replication, histone mRNA expression is controlled by a 3′-end stem-loop structure unique to replication-dependent histone mRNAs. In *Drosophila*, this regulation is mediated by histone mRNA stem-loop–binding protein (dSLBP), which has minimal tertiary structure when not bound to RNA. We show here that phosphorylation of dSLBP dramatically increases binding affinity for stem-loop RNA. The phosphorylated C-terminal tail of dSLBP does not contact RNA. Instead, increased negative charge on the C-terminal tail and stabilization of structural elements by a phosphorylation site within the RNA-binding domain promote more compact conformations that should reduce the entropic barrier to binding histone mRNA.

Author contributions: J.Z., D.T., E.F.D., L.P., Z.D., W.F.M., L.T., and T.M.T.H. designed research; J.Z., D.T., E.F.D., and L.P. performed research; J.Z., D.T., E.F.D., L.P., Z.D., W.F.M., L.T., and T.M.T.H. analyzed data; and J.Z., D.T., E.F.D., L.P., Z.D., W.F.M., L.T., and T.M.T.H. wrote the paper.

The authors declare no conflict of interest.

This article is a PNAS Direct Submission.

Data deposition: The crystallographic coordinates and structure factors have been deposited with the Research Collaboratory for Structural Bioinformatics Protein Data Bank [accession nos. 4QOZ - hSLBP RPD:RNA:3′hExo, 4TV0 - dSLBP RPD-5E (L245M, L253M), 4TUW - dSLBP RPD-5E, and 4TUX - dSLBP RPD-wt].

[1]To whom correspondence may be addressed. Email: marzluff@med.unc.edu, ltong@columbia.edu, or hall4@niehs.nih.gov.

This article contains supporting information online at www.pnas.org/lookup/suppl/doi:10.1073/pnas.1406381111/-/DCSupplemental.

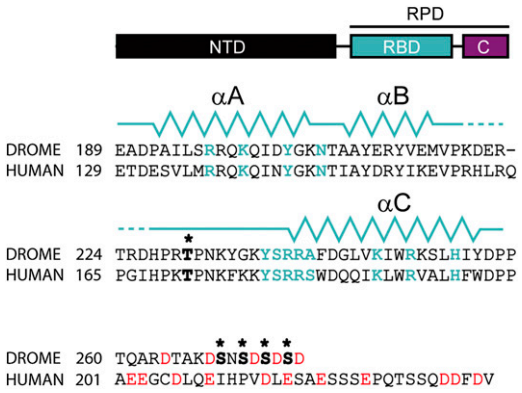

Fig. 1. Schematic of the domain architecture of dSLBP (*Upper*) and amino acid sequence alignment of RPDs of *Drosophila* and human SLBP (*Lower*). Domains of SLBP include the N-terminal domain (NTD), RBD, and C-terminal region (C). Amino acid sequences are shown with the RBD sequence in the top two rows and the C-terminal region in the bottom row. T230 in the TPNK motif and phosphorylation sites in the C-terminal region are indicated with boldface and asterisks, respectively; the residues involved in RNA binding are shown in cyan; and acidic residues in the C-terminal region are shown in red.

RNA-binding domain, but the C-terminal region is flexible in the protein:RNA complex and does not contact the RNA. Instead, we show that the increased negative charge in the C-terminal region of the dSLBP RPD results in a more compact ensemble of protein conformations in the absence of RNA, thereby increasing RNA-binding affinity by reducing the entropy of the unbound protein.

Results

Phosphorylation Promotes SLBP RNA-Binding Affinity. We measured the RNA-binding affinity of dSLBP at equilibrium and discovered markedly increased binding affinity with phosphorylation. Full-length dSLBP bearing phosphorylation at up to seven sites, including the TPNK motif and C-terminal tail, bound to the histone mRNA stem loop with a K_d of ~0.5 ± 0.07 pM (Table 1 and Fig. S1*A*). Partial dephosphorylation of dSLBP (*Materials and Methods*) decreased affinity by 250-fold (Table 1 and Fig. S1*A*). To evaluate the effects of added negative charge at the TPNK and C-terminal phosphorylation sites separately or in combination, we turned to *Escherichia coli*-expressed fragments of the dSLBP RPD with Glu residues mimicking phosphorylation. We could produce these phosphorylation mimics in sufficient quantities for biochemical and structural studies, but we could produce only limited amounts of phosphorylated proteins for binding assays. We engineered three dSLBP RPD mutants to mimic phosphorylation: dSLBP RPD-EPNK to mimic TPNK motif phosphorylation; dSLBP RPD-4E, in which four Ser-to-Glu mutations mimic phosphorylation of the C-terminal region; and dSLBP RPD-5E, bearing the EPNK mutation plus the four Ser-to-Glu mutations in the C-terminal region.

Table 1. In vitro binding of dSLBP to the histone mRNA stem loop

	K_d, nM
Phosphorylated dSLBP	0.0005 ± 0.00007
Dephosphorylated dSLBP	0.14 ± 0.01
dSLBP RPD-WT	46.1 ± 2.8
dSLBP RPD-5E	0.098 ± 0.01
dSLBP RPD-EPNK	17.2 ± 3.4
dSLBP RPD-4E	4.04 ± 1.4
Phosphorylated dSLBP RPD-EPNK	0.0012 ± 0.0003

dSLBP RPD-5E bound the histone mRNA stem loop >400-fold more tightly than the nonphosphorylated dSLBP RPD, mirroring the increase in binding affinity observed with the full-length phosphorylated dSLBP (Table 1 and Fig. S1*A*). dSLBP-EPNK bound to stem-loop RNA threefold more tightly than nonphosphorylated dSLBP RPD-WT, in accordance with a previous report where phosphorylation of the TPNK motif increased binding affinity sevenfold (16). dSLBP RPD-4E bound to stem-loop RNA 12-fold more tightly than did dSLBP RPD-WT. Thus, the combination of increased negative charge at both positions resulted in a synergistic increase in binding affinity. We further confirmed the major role of C-terminal tail phosphorylation by

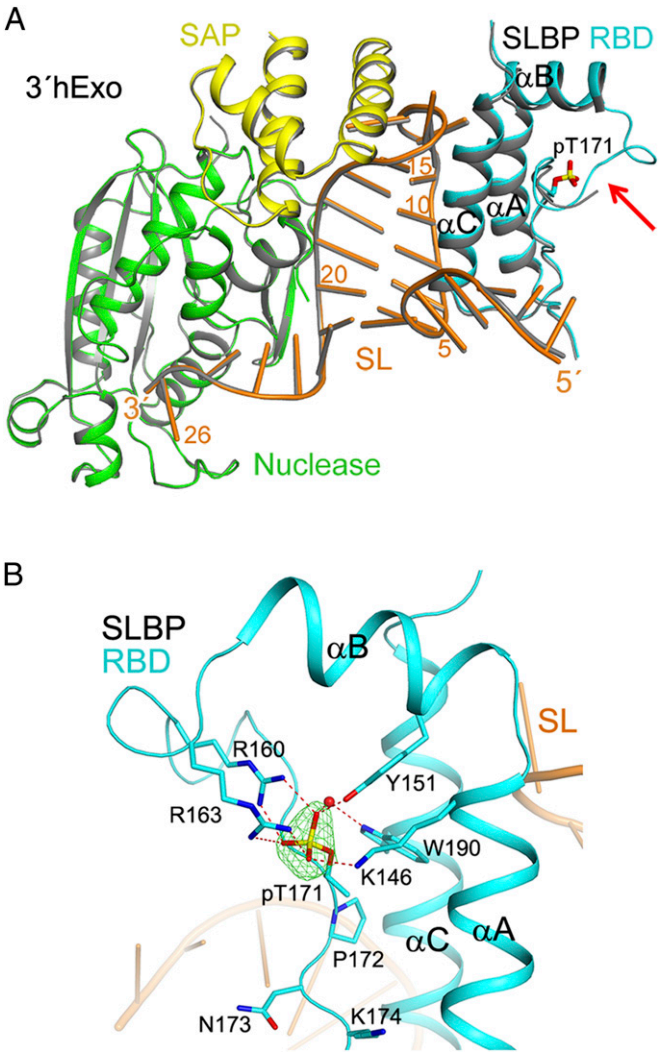

Fig. 2. Crystal structure of the phosphorylated hSLBP RBD-pT171 in complex with the histone mRNA stem loop and 3′hExo. (*A*) Superposition of the crystal structure of the human histone mRNA stem loop (orange), hSLBP RBD-pT171 (cyan), and 3′hExo (green nuclease domain and yellow SAP domain) ternary complex with that of the unphosphorylated ternary complex (gray) (18). The red arrow points to the loop region that is disordered in the unphosphorylated complex. (*B*) Interaction of hSLBP side chains with pT171. Hydrogen bonds and salt bridges involving the phosphate group on T171 are shown by red dashes. The red sphere is a water molecule that interacts with both W190 and the phosphate group. Simulated annealing omit F_{obs}–F_{calc} electron density for the phosphate is shown also, contoured at 3σ. Equivalent residues in hSLBP/dSLBP are as follows: T171/T230, K146/K206, Y151/Y211, R160/K220, R163/R223, and W190/W249. This figure, Figs. 3 and 6*F*, and Figs. S3 and S6 were created with PyMOL (Schrödinger).

Table 2. Data collection and refinement statistics

	hSLBP RBD pThr171-SL-3′hExo	dSLBP RPD-5EL245M/L253M	dSLBP RPD-5E	dSLBP RPD-WT
Data collection				
Space group	$P2_12_12_1$	$P4_132$	$P4_32_12$	$P4_32_12$
Cell dimensions				
a, *b*, *c*, Å	82.1, 91.5, 128.7	103.9, 103.9, 103.9	74.8, 74.8, 161.3	75.0, 75.0, 173.5
α, β, γ, °	90, 90, 90	90, 90, 90	90, 90, 90	90, 90, 90
Resolution, Å	50.0–2.3 (2.38–2.30)	50–2.6 (2.64–2.60)	50–2.9 (3.0–2.9)	50–3.08 (3.15–3.10)
R_{sym} or R_{merge}	0.092 (0.48)	0.099 (0.65)	0.144 (0.47)	0.099 (0.50)
I/σI	9.5 (1.8)	26.7 (2.6)	13.6 (3.0)	33.7 (2.6)
Completeness, %	93.2 (84.5)	99.8 (99.5)	97.6 (81.6)	93.4 (60.4)
Redundancy	3.5 (3.5)	23.8 (6.2)	7.2 (5.5)	12.3 (6.8)
Refinement				
Resolution, Å	38.2–2.3	46.5–2.6	23.7–2.9	45.8–3.08
No. reflections	40,611	11,133	10,448	9,127
R_{work}/R_{free}	19.3/24.5	25.0/28.7	21.5/26.3	25.5/31.7
No. atoms	6,416	926	2,282	2,215
Protein	5,201	384	1,157	1,135
RNA	918	540	1,120	1,076
Water/ion	297	2	5	4
B-factors				
Protein	25.5	50.0	72.7	110.0
RNA	38.4	66.8	72.1	113.4
Water/ion	28.5	81.7	91.8	108.8
Rms deviations				
Bond lengths, Å	0.008	0.007	0.008	0.016
Bond angles, °	1.1	1.2	1.2	1.4

Values in parentheses are for highest-resolution shell.

determining the binding affinity of dSLBP RPD-EPNK whose C-terminal tail was phosphorylated in vitro (K_d ~1.2 ± 0.25 pM) (Table 1). The RNA-processing domain alone binds almost as tightly as full-length phosphorylated dSLBP. Although phosphorylated dSLBP RPD-EPNK bound to stem-loop RNA 40-fold more tightly than the phosphorylation mimic dSLBP RPD-5E, a dramatic increase in RNA-binding affinity was observed for both proteins. Given the homogeneity and availability of sufficient quantities of the dSLBP RPD-5E mimic, we used this protein for additional studies. C-terminal phosphorylation appears unique to dSLBP, with SLBP from all sequenced *Drosophila* species ending in an SD-rich region, and the dramatic increase in affinity with C-terminal tail phosphorylation or phosphorylation mimicry supports its previously demonstrated importance for biological activity (15).

Phosphorylation of SLBP at the TPNK Motif Stabilizes Interactions Between Structural Elements. A 2.3-Å–resolution crystal structure of the hSLBP RBD phosphorylated at the TPNK motif in a ternary complex with 3′hExo and the histone mRNA stem loop demonstrates that phosphorylation at the TPNK motif stabilizes structural elements in SLBP (Fig. 2*A* and Table 2). The phosphate on T171, located away from the protein:RNA interface, interacts with the side chains of K146, Y151, R160, R163, and Y190 (Fig. 2*B*), bringing together the three α-helices (αA–αC) and the long αB–αC loop of the RBD. The beginning of the αB–αC loop (residues P159–Q164), which was disordered in the structure with nonphosphorylated SLBP, now is completely structured. Surprisingly, there were minimal overall structural changes in the ternary complex with TPNK phosphorylation compared with the complex without phosphorylation (18) (Fig. 2*A*), with an rmsd of 0.2 Å for equivalent Cα atoms in hSLBP excluding residues 165–169, and an rmsd of 0.3 Å for 3′hExo. However, the interactions with the phosphate group are important for SLBP function, because Y151F and K146A mutations in human SLBP were shown to reduce RNA-binding and/or histone mRNA-processing activity in vitro (19).

Because human SLBP lacks the C-terminal phosphorylation sites that dramatically influence binding affinity, we also determined crystal structures of the dSLBP RPD in complex with the histone mRNA stem loop (Fig. 3*A* and Table 2) (18). Unexpectedly, the C-terminal region was disordered in structures of dSLBP with or without phosphorylation mimicry (dSLBP RPD-5E and dSLBP RPD-WT, respectively). However, the overall structures of the dSLBP RBD and stem-loop RNA and the critical protein:RNA contacts are similar to each other and to that of hSLBP, with an rmsd of 0.6 Å over all 405 protein and 411 RNA atoms (Fig. 3*B* and Fig. S2). In complexes with hSLBP and/or 3′hExo [Protein Data Bank (PDB) ID code: 4L8R] (18), the histone mRNA stem-loop structure is different from that

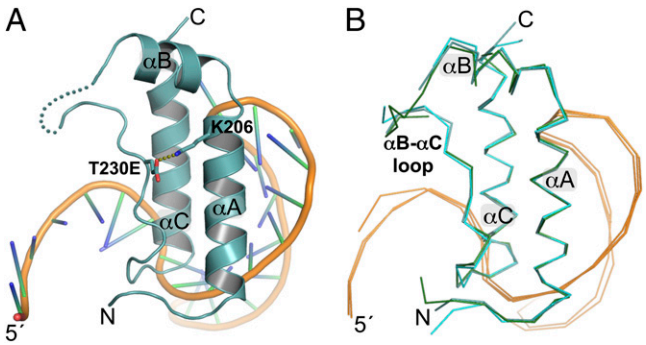

Fig. 3. Crystal structures of dSLBP RPD in complex with the histone mRNA stem loop. (*A*) Ribbon diagram of dSLBP RPD-5E in complex with the histone mRNA stem loop. A disordered region in the αB–αC loop (K220–T224) is indicated by small spheres. (*B*) Superposition of the crystal structures of protein:RNA complexes of dSLBP RPD-5E (aqua), dSLBP RPD-WT (green), and hSLBP RPD. (PDB ID code 4HXH is shown in cyan).

found in solution (PDB ID codes: 1JWC and 1KKS) (20, 21). Strikingly, in the dSLBP:RNA crystal structures, the stem-loop RNA has essentially the same structure as in the human SLBP:RNA:3′hExo or 3′hExo:RNA complexes, despite different crystal packing environments and the absence of crystal contacts in the RNA loop region. Thus, both SLBP and 3′hExo induce the same structural changes in the RNA when they bind the stem loop, and as a consequence each may initiate complex formation on the histone mRNA.

At 2.6-Å resolution the crystal structure of the dSLBP RPD-5E mutant indicates that the EPNK motif contributes an interaction equivalent to one of those observed for hSLBP with phosphorylated Thr. A salt bridge is formed between T230E in the EPNK motif and K206, which is equivalent to K146 in hSLBP (Fig. 3*A*). All the phosphate-interacting residues identified in hSLBP are conserved in dSLBP, and many of the interactions with the phosphate group are observed in a molecular dynamics simulation of the phosphorylated TPNK dSLBP RPD (Fig. S3), suggesting that the equivalent stabilizing interactions are conserved in dSLBP. The phosphorylation-dependent interactions identified in hSLBP and predicted by the crystal structure and molecular dynamics simulation of dSLBP provide a structural explanation for the three- to sevenfold increase in RNA-binding affinity caused by TPNK motif phosphorylation.

The dSLBP C-Terminal Region Is Flexible in a Protein:RNA Complex. We turned to NMR studies to characterize the structural effects of the dSLBP C-terminal tail and found that RNA binding induces the transition of the dSLBP RPD from an unstructured to a structured state, irrespective of the charge state of the C-terminal region. Superposition of ^{15}N-heteronuclear single quantum coherence (HSQC) spectra of the dSLBP RPD-5E phosphorylation mimic in the free and RNA-bound states showed significant chemical shift perturbation (Fig. 4*A*). In the free state, resonances for dSLBP RPD-5E had narrow chemical shift dispersion, centered around 8.0 ppm for amide groups (Fig. 4*A*) and 0.8 ppm for methyl groups (Fig. 4*B*), indicating that the protein exists as a rapidly interchanging ensemble of conformations. Upon RNA binding, well-dispersed chemical shifts were observed for both amide and methyl groups. The ^{15}N-HSQC spectrum of the RNA-bound TPNK phosphorylation mimic, dSLBP RPD-EPNK, is very similar to that of RPD-5E:RNA (Fig. S4), indicating that the structure of the dSLBP RPD:RNA complex in solution does not change with increased negative charge in the C-terminal region of the dSLBP RPD-5E mutant.

The ^{15}N-HSQC spectra of the dSLBP RPD-5E and dSLBP RPD-EPNK complexes with RNA, like the crystal structures, indicate that the C-terminal region is unstructured when dSLBP is bound to the histone mRNA stem loop. The average amide peak intensities of the C-terminal region for both mutants were 10-fold stronger than those of the dSLBP RBD (Fig. 4*C* and Fig. S5). This distinction in intensity of peaks for the RBD (residues 189–259) and the C-terminal region (residues 260–276) suggests that the two regions have different effective rotational correlation times and that the dSLBP RBD:RNA complex behaves as a 16-kDa moiety, whereas the C-terminal region behaves as a separate 1.6-kDa moiety (Fig. 1*A*). Based on this observation, it is unlikely that the C-terminal tail, phosphorylated or not, contacts the dSLBP RBD:RNA complex. The NMR and crystallography results concur, suggesting that the phosphorylation status of the C-terminal tail does not change the core structure of dSLBP and that the C-terminal tail is flexible in a complex with RNA. Thus, it appears the negatively charged C-terminal tail increases dSLBP binding affinity by 150-fold without contacting the RNA.

The Role of Entropy in Increased RNA-Binding Affinity Caused by Phosphorylation Mimicry. We performed isothermal titration calorimetry (ITC) experiments with the phosphorylation mimics, dSLBP RPD-5E and RPD-EPNK and found that the thermodynamic origin of the dramatically increased RNA-binding affinity caused by the negative charge of the C-terminal tail is primarily entropic. The tight binding of dSLBP RPD-5E (K_d = 100 pM) prevented us from characterizing a titration curve using ITC. Nevertheless, we measured the total heat release with a single injection (Fig. 5*A*). We found that the difference in heat release upon RNA binding for dSLBP RPD-EPNK (−24.7 ± 0.9 kcal/mol) vs. dSLBP RPD-5E (−23.0 ± 0.7 kcal/mol) was not significant, suggesting that the total enthalpy change is the same for both proteins. We therefore ascribe the 150-fold difference in RNA-binding affinity for dSLBP RPD-5E vs. RPD-EPNK (a change of 2.8 kcal/mol) to the entropic term. Given the flexibility of the C-terminal region when bound to RNA, we hypothesize that phosphorylation of the dSLBP C-terminal tail may increase RNA-binding affinity by stabilizing RNA-binding–competent conformations before binding, thereby decreasing conformational entropy.

Phosphorylation Mimicry on the C-Terminal Tail Makes SLBP More Compact in the Absence of RNA. Our hypothesis that C-terminal tail phosphorylation stabilizes RNA-binding–competent conformations implies that the ensemble of conformations is more compact. We therefore used FRET and showed that C-terminal phosphorylation mimicry decreases the molecular dimensions of the dSLBP RBD. The dSLBP RBD has seven Tyr residues scattered throughout the domain and a single Trp residue, W249 (Fig. S6). Tyr fluorescence emission overlaps the absorption spectrum of Trp. Thus, W249 is an acceptor for the energy from the Tyr residues. We excited the Tyr residues at 270 nm and monitored Tyr emission at 300 nm and Trp emission at 350 nm at different urea concentrations (Fig. 5 *B* and *C*). FRET efficiency (assessed by the ratio of Tyr emission to Trp emission) is proportional to the compactness of the RBD (22).

For both dSLBP RPD-EPNK and RPD-5E proteins, Tyr fluorescence increased in the presence of 7.5 M urea (Fig. 5*C*). The sensitivity of Tyr fluorescence at ∼300 nm to increasing urea concentration indicated residual structure within both phosphorylation mimics of the dSLBP RPD, as previously shown by CD studies (14). The degree of change was small because of the long Foster range (∼18 Å) and high background of Tyr/Trp FRET (22), but the difference was reproducible. Tyr emission at 300 nm was lower for dSLBP RPD-5E than for RPD-EPNK at all urea concentrations, indicating more compact conformations for the C-terminal tail phosphorylation mimic. Furthermore, the emission peak of Trp shifts toward shorter wavelength (blue shift) in a hydrophobic environment or toward a longer wavelength (red shift) in a polar environment, and the Trp emission peak for dSLBP RPD-5E was at a shorter wavelength than that of dSLBP RPD-EPNK at 0 M urea (Fig. 5*C*). We also observed a red shift for both dSLBP RPD-5E and RPD–EPNK in 7.5 M urea, indicating that W249 became more exposed to solvent at higher urea concentrations. The FRET efficiency suggests that the molecular dimensions of dSLBP RPD-EPNK in the absence of urea are equivalent to those of dSLBP RPD-5E in 3 M urea. Thus, we conclude from these fluorescence data that mimicking phosphorylation of the C-terminal region makes the dSLBP RPD more compact.

Localization of the C-Terminal Tail of dSLBP in Free and RNA-Bound Forms. Paramagnetic relaxation enhancement (PRE) provides a method to characterize the localization of the C-terminal region with respect to the dSLBP RBD in both free and RNA-bound states (Fig. 6). MTSL [*S*-(2,2,5,5-tetramethyl-2,5-dihydro-1*H*-pyrrol-3-yl)methyl methanesulfonothioate], a paramagnetic

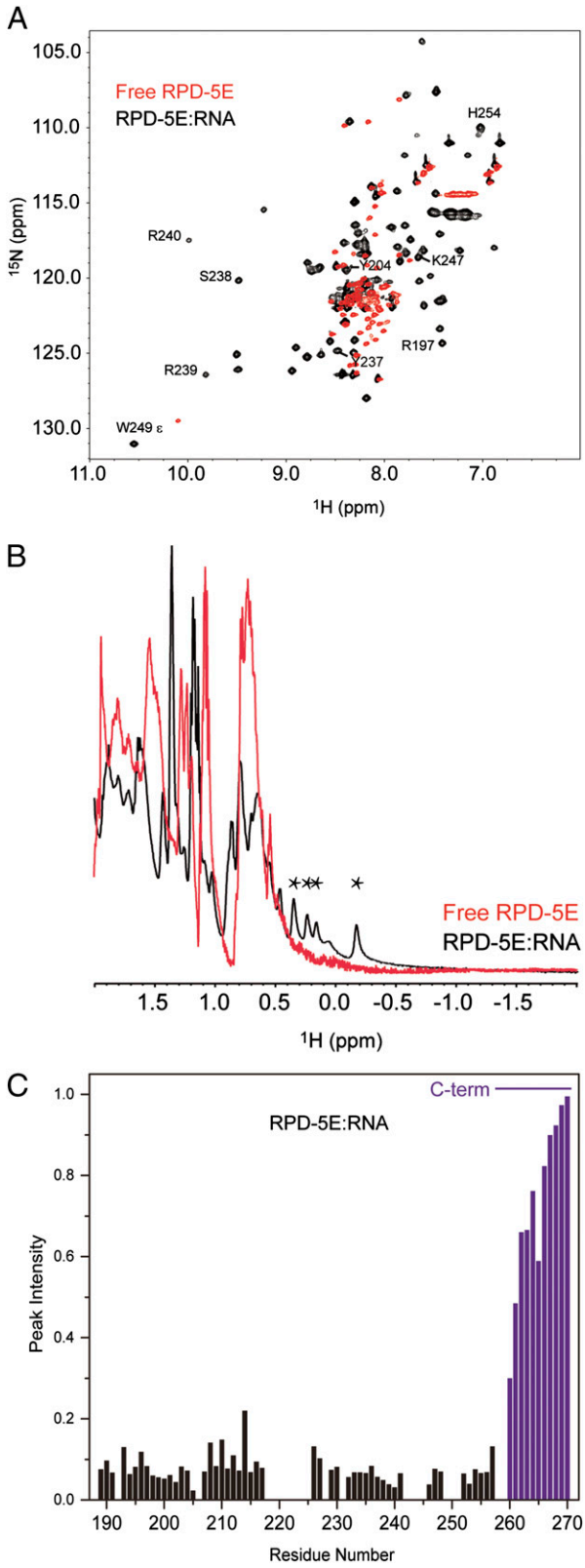

Fig. 4. NMR analysis of the dSLBP RPD-5E:RNA complex. (*A*) ^{15}N-HSQC of free (red) and RNA-bound (black) dSLBP RPD-5E. For clarity, only the assignments for the residues involved in RNA binding are labeled. (*B*) Methyl regions of the 1D-^{1}H spectrum of free (red) and RNA-bound (black) dSLBP RPD-5E. Peaks for methyl groups shifted to high field are starred. (*C*) Plot of relative peak intensities of ^{15}N-HSQC of RNA-bound dSLBP RPD-5E, as shown in *A*. The C-terminal region (C-term) is denoted by the purple bar. The peak intensities of unassigned residues are not shown and appear as gaps in the histogram.

compound, was covalently attached to a cysteine residue added to the C-terminal end of the dSLBP RPD. MTSL attenuates the resonances of surrounding residues in a distance-dependent manner. PRE is quantified by determining the ratio of the intensities of resonances in the paramagnetic state to their intensity in the diamagnetic state (I_{para}/I_{dia}). A value close to 0 correlates with high proximity to the paramagnetic compound (<12 Å), and values approaching 1 indicate low proximity (>25 Å) (23). In the RNA-bound state, only a few resonances outside the C-terminal region of dSLBP RPD-5E and RPD-EPNK were attenuated (Fig. 6 *A* and *B*), confirming our structural observations that the C-terminal region does not contact the core RNA-binding domain in the protein:RNA complex.

In contrast, in the absence of RNA, both dSLBP RPD-5E and RPD-EPNK showed ubiquitous perturbations caused by the spin label at the C terminus (Fig. 6 *C* and *D*), indicating that the free dSLBP RPD exists as an ensemble of quickly interconverting conformers, in accordance with previous studies (14). Furthermore, this perturbation pattern is distinct from the pattern of a fully unfolded protein in which perturbations would be confined to resonances near the spin label in the primary sequence (24). It is noteworthy that the side chain of W249 in the hydrophobic core was bleached completely, as is consistent with the residual structure. Decreased average PRE values in the absence of RNA (~0.3, compared with 0.86 in the RNA-bound state) are consistent with the C-terminal region interacting with the core RBD in the unbound form.

A comparison of the perturbation patterns of dSLBP RPD-5E and RPD-EPNK indicates that overall conformational freedom is lower for dSLBP RPD-5E than for RPD-EPNK and suggests a set of basic residues that may interact with the phosphorylated tail. In general, we observed greater perturbation (negative ΔPRE values) for resonances in dSLBP RPD-EPNK than in RPD-5E, as is consistent with more conformational freedom in the RPD in the absence of the added negative charge in the C-terminal region (Fig. 6*E*). A small number of resonances were more greatly perturbed in the dSLBP RPD-5E mutant (more positive ΔPRE values), indicating that on average the corresponding residues were nearer the C-terminal tail. We mapped several of these resonances to the N-terminal part of helix αA (Fig. 6*F*); this location suggests that these residues (S196, R197, R198) interact with the phosphorylated C-terminal tail in the absence of RNA. Another Ser-Arg-Arg sequence (S238, R239, R240), which recognizes G9 in the histone mRNA (Fig. S2), is found in the N-terminal part of helix αC, but we were unable to assign these resonances. Both Ser-Arg-Arg motifs interact with the stem of the histone mRNA stem loop, and three of the four arginine residues are located near each other in the complex with RNA (Fig. 6*F*). We propose that in the absence of RNA the phosphorylated C-terminal tail of the dSLBP RPD interacts with these two Ser-Arg-Arg motifs and other basic residues on the RNA-binding surface (e.g., K247, R250, K251) through transient salt bridges. The negative charge counterbalances the positive charges to allow helices αA and αC to come together and may stabilize a nascent RNA-binding structure.

In support of the hypothesis that phosphorylation promotes unbound protein compaction, molecular dynamics simulation of the structures of the fully phosphorylated dSLBP RPD (Movie S1) or TPNK-phosphorylated dSLBP RPD (Movie S2) in the absence of RNA showed the phosphorylated C-terminal tail to be less dynamic than in its nonphosphorylated form. To characterize the impact of phosphorylation of the C-terminal tail on protein dynamics quantitatively, we calculated the backbone

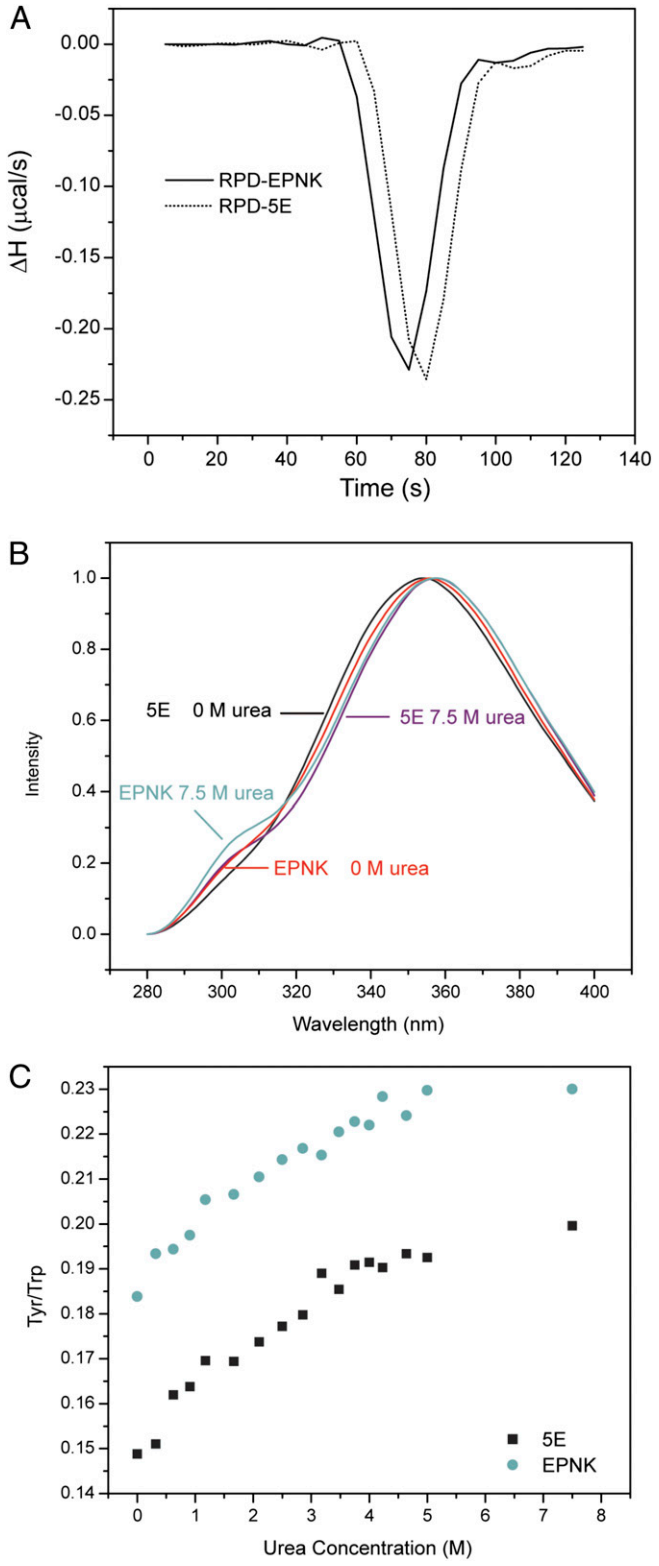

Fig. 5. ITC and FRET studies of dSLBP RPD. (*A*) ITC measurements of histone mRNA stem-loop binding for dSLBP RPD-EPNK and dSLBP RPD-5E. Representative curves are shown. (*B*) Representative fluorescence emission curves of free dSLBP RPD-5E and dSLBP RPD-EPNK at 0 and 7.5 M urea. Curves for dSLBP RPD-5E are shown in black (0 M urea) and purple (7.5 M urea), and curves for dSLBP RPD-EPNK are shown in aqua (0 M urea) and red (7.5 M urea). The curves are normalized to the emission of W249. (*C*) Ratio of Tyr/Trp emission with increasing urea concentration for free dSLBP RPD-5E and dSLBP RPD-EPNK.

amide order parameters (S^2) from the last 60 ns of the molecular dynamics trajectory. The order parameter is a measure of the degree of spatial restriction or protein rigidity, with values ranging from 0 (most flexible) to 1 (most rigid) (25). In general, phosphorylation rigidifies dSLBP RPD with large effects on the C-terminal tail and a portion of the αB–αC loop, which was disordered in the crystal structures of the dSLBP RPD (Fig. S7).

Discussion

Roles of C-Terminal Region Phosphorylation in Histone mRNA Binding. The RBD of dSLBP is rich in basic amino acids with helix αA, the αB–αC loop, and helix αC bearing +3, +3, and +4 net positive charges, respectively. Because these three structural elements pack together in the RNA-bound structure, the positive charges must be neutralized to accomplish protein folding. Our results and a previous circular dichroism study suggesting the existence of α-helices (14) indicate that the dSLBP RPD possesses a transient residual tertiary structure in the absence of added negative charge at the C-terminal tail. Thus, dSLBP bears the characteristics of the so-called "molten globule." Our crystal structure of hSLBP RBD-pT171 suggests that phosphorylation of the TPNK motif may stabilize RNA-binding–competent conformations by bringing together helices αA and αC and the long αB–αC loop.

Phosphorylation of the C-terminal tail balances the positive charges in the RBD and allows the formation of RNA-binding–competent conformations. Phosphorylation of up to four Ser residues in the C-terminal tail of dSLBP adds up to eight negative charges, in addition to the negative charges from the five Asp residues in the tail. The paramagnetic perturbation of the dSLBP RBD in the absence of RNA suggests that the C-terminal tail associates with helices αA and αC as the RNA-binding surface is forming and is displaced when RNA is bound. The repetitive pattern of the phosphorylation sites with acidic residues provides multiple configurations for transient interactions with basic residues on αA and αC. Together with phosphorylation of the TPNK motif, this stabilized nascent conformation increases RNA-binding affinity more dramatically (400-fold higher than in the absence of phosphorylation mimicry), apparently by reducing the entropic barrier to binding.

The C-terminal region of human SLBP is not phosphorylated, although its RBD also is rich in basic residues (Fig. 1). However, the more extended C-terminal region of hSLBP is rich in acidic amino acid residues: 11 of the 36 residues in the minimal protein that is fully proficient in processing are acidic. The first three acidic residues are conserved in mammals, chick, frog, and fish, and six of the remaining eight are conserved in the five mammals (human, chimp, dog, mouse, and rat). These acidic residues may substitute functionally for the phosphorylated C-terminal tail of dSLBP, although their charge cannot be regulated. SLBP is present only in S-phase in mammals (26) and hence always is needed in an active form. In contrast, dSLBP is not degraded rapidly at the end of S phase (27). Thus, modulating C-terminal phosphorylation of dSLBP may provide a means of regulating its activity outside of S phase.

Our results together with previous studies (10, 15) suggest a model for how phosphorylation of dSLBP may coordinate the initial events of histone pre-mRNA processing (Fig. 7). Non-phosphorylated dSLBP exists as an ensemble of unstructured conformations with high flexibility. Similarly, the histone mRNA stem loop may exist in multiple conformations. Phosphorylation of the C-terminal tail reduces electrostatic repulsion and compacts the structure by drawing together αA and αC to prepare dSLBP for RNA binding (Fig. 6). Phosphorylation at the TPNK motif, which is essential for viability of flies (28), may further stabilize interactions between αA, αB, and the αB–αC loop. As a result of these synergistic transitions, the sampling space for protein conformation is greatly reduced, with a concomitant

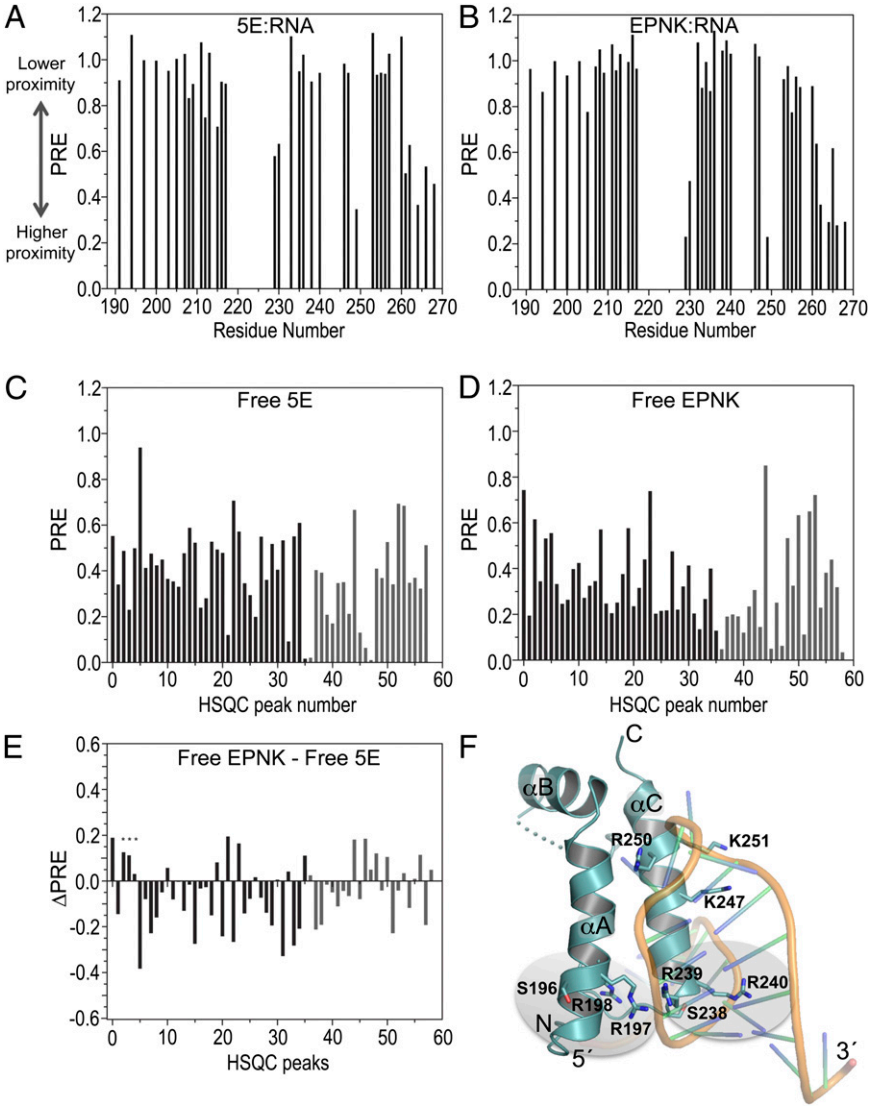

Fig. 6. PRE study of dSLBP RPD. PRE ratios are plotted for RNA-bound and free dSLBP RPD: (*A*) RNA-bound RPD-5E, (*B*) RNA-bound RPD-EPNK, (*C*) free RPD-5E, and (*D*) free RPD-EPNK. PRE values for unassigned residues in *A* and *B* are not shown. Resonances were partially assigned for *C* and *D*; the assigned peaks are shown in black and the unassigned peaks are shown in gray. (*E*) Plot of differences between PRE ratios for free dSLBP RPD-EPNK and dSLBP RPD-5E. (*F*) Location of residues with positive PRE ratio differences, as shown in *E*. A ribbon diagram of dSLBP RPD-5E in complex with histone mRNA stem loop is shown displaying side chains for a Ser-Arg-Arg motif, S196, R197, and R198 (gray oval), whose assigned resonances have positive ΔPRE ratios. Side chains for a second Ser-Arg-Arg motif (gray oval) and additional basic residues on the RNA-binding surface are shown also.

reduction in the entropic penalty for RNA binding resulting in a dramatic increase in dSLBP's RNA-binding affinity. Upon RNA binding, the release of the phosphorylated C-terminal tail from the RNA-interacting surface also increases entropy, and the protein and RNA achieve the stable conformations observed in crystal structures.

Following RNA binding, an additional role for the released phosphorylated C-terminal tail may be to recruit or activate downstream processing factors and/or to function in other aspects of histone mRNA metabolism (e.g., transport, translation, or mRNA degradation). In *Drosophila*, there is no histone pre-mRNA cleavage until dSLBP binds (10). The free phosphorylated C-terminal tail of dSLBP could assist in assembling a processing complex after it has promoted binding to the stem-loop RNA. The SLBP:RNA complex is long lived with undetectable dissociation in vitro (29), suggesting that the phosphorylated tail is available to bind to other factors. Furthermore, the histone stem-loop RNA conformation with dSLBP differs from that of unbound RNA (20, 21). Stabilization of the stem-loop RNA structure is consistent with the fact that the initial binding event in the cell is SLBP binding to the histone pre-mRNA (30). Thus, both the free C-terminal tail and RNA conformational change may contribute to the recruitment of additional factors for histone mRNA regulation.

The modulation of conformational entropy by phosphorylation that we observed with dSLBP may apply to other RNA-binding proteins with intrinsically disordered regions adjacent to RBDs. For example, Ser/Arg-rich proteins possess Arg-Ser (RS) repeats that may be phosphorylated, and these repeats often are adjacent to an RNA-recognition motif (RRM) or other RBDs. Ser/Arg-rich splicing factor 1 (SRSF1) contains two N-terminal RRMs followed by C-terminal RS repeats. The RS region appears to interact intramolecularly with its RRM domains in the nonphosphorylated state, but phosphorylation of the RS C-terminal tail promotes dissociation from the RRM domains to allow intermolecular interactions of both the RRM and RS regions with

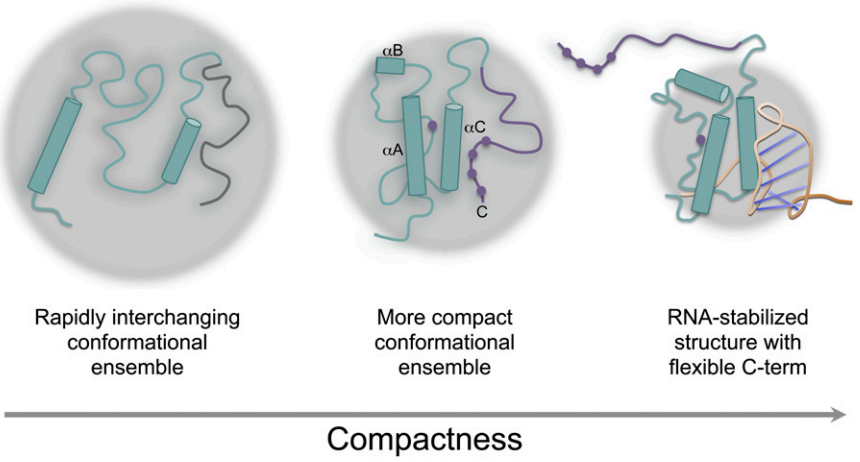

Fig. 7. Model for phosphorylation-stimulated binding of dSLBP to the histone mRNA stem loop. Nonphosphorylated (WT) dSLBP exists as an ensemble of conformations (*Left*) that becomes more compact upon phosphorylation (indicated by purple spheres) of the TPNK motif and C-terminal tail (*Center*). The phosphorylated C-terminal tail is flexible upon RNA binding and available to bind other molecules (*Right*).

additional splicing factors (31). In addition, phosphorylation of the RS region has been shown to stabilize its structure and decrease its conformational entropy (32). In this case, the decreased conformational entropy of the free, phosphorylated RS tail favors protein–protein interactions in the early steps of spliceosome assembly. It has not yet been established whether conformational entropy modulates RNA target binding by SRSF1, but the arrangement of RNA-binding domains adjacent to an unstructured phosphorylated region in SRSF1 and in other RBD proteins suggests that other proteins also use the mechanism we found for dSLBP.

Materials and Methods

Protein Constructs and Purification. Phosphorylated hSLBP RBD-pT171 was expressed in baculovirus-infected insect cells and purified as described previously for unphosphorylated SLBP (18). His-tagged phosphorylated full-length dSLBP was expressed in baculovirus-infected cells as described previously (33) and contained four to seven phosphates. Full-length dSLBP protein was partially dephosphorylated by incubating His-tagged full-length dSLBP (~0.5 mg) with 50 units of alkaline phosphatase (CIP; New England Biolabs) in 1× CutSmart buffer for 3 d at room temperature. The treated sample was repurified on Ni-NTA resin and further purified using a Superdex 200 column equilibrated with 20 mM Hepes (pH 7.5), 500 mM NaCl. The degree of dephosphorylation was estimated by mass spectrometry: ~12% was completely dephosphorylated, ~38% was monophosphorylated, and ~50% was doubly phosphorylated.

A cDNA encoding the RPD of *Drosophila melanogaster* SLBP (residues 184–276) was subcloned into pSMT3 with an N-terminal small ubiquitin-related modifier (SUMO) tag (Invitrogen). The phosphorylation mimic mutants (5E:T230E/S269E/S271E/S273E/S275E, 4E:S269E/S271E/S273E/S275E, EPNK:T230E) and methionine mutant (L245M/L253M) were created by site-directed mutagenesis PCR with the mutations encoded in corresponding primers. *E. coli* BL21 (DE3) CodonPlus cells transformed with expression plasmid were grown at 37 °C in LB medium to an OD_{600} of 0.6. The cell cultures then were transferred to 20 °C, 0.4 mM isopropyl-1-thio-β-D-galactopyranoside was added, and incubation was continued overnight for protein expression. The cells were harvested by centrifugation, and pellets were stored at −80 °C until use.

All dSLBP proteins were purified by the same procedure at 4 °C. The cell pellet was resuspended in 20 mM Tris·HCl (pH 8.0), 1 M NaCl, 0.1% (vol/vol) Triton X-100, 25 mM imidazole, and 1 mg/mL lysozyme and was subjected to three freeze-thaw cycles followed by sonication. The soluble fraction was applied to a Ni^{2+}-NTA affinity column and thoroughly washed with 20 mM Tris·HCl (pH 8.0), 1 M NaCl, and 1 mM Tris (2-carboxyethyl) phosphine hydrochloride (TCEP). The target SUMO fusion protein was eluted with column buffer containing 250 mM imidazole and cleaved overnight with 0.1 mg of Ubl-specific protease 1. The cleaved fusion protein sample was applied to a heparin affinity column and eluted with a linear gradient from 0–2 M NaCl in 20 mM Tris·HCl (pH 8.0). SUMO and dSLBP RPD eluted at 160 mM and 400 mM NaCl, respectively. The dSLBP RPD was purified further using a Superdex 75 column equilibrated with 20 mM Hepes (pH 7.5), 500 mM NaCl. Selenomethionine (SeMet)-labeled protein was prepared including TCEP in all buffers. dSLBP RPD-EPNK was phosphorylated with casein kinase II (New England Biolabs) in 20 mM Tris·HCl (pH 7.5), 50 mM KCl, 10 mM $MgCl_2$, and 1 mM ATP for 2 d at 25 °C. The phosphorylated protein was purified further using the protocol used for WT SLBP.

EMSA. The histone mRNA stem loop was labeled at the 5′ end with ^{32}P-γ-ATP (PerkinElmer Life Science) by T4 polynucleotide kinase for 1 h at 37 °C. Unreacted ^{32}P-γ-ATP was removed with Illustra MicroSpin G-25 columns. Radiolabeled RNA (<50 pM for dSLBP RPD-WT and dSLBP RPD–EPNK or <1 pM for all others) was incubated with serially diluted concentrations of protein at 4 °C for 36 h in 10 mM Hepes, 100 mM NaCl, 0.01% (vol/vol) Tween 20, 0.1 mg/mL BSA, and 20 μg/mL yeast tRNA. The protein:RNA samples were run on 10% native PAGE gels at a constant voltage (150 V) with 1× Tris-borate-EDTA buffer at 4 °C for 20 min. The gels were dried and exposed to storage phosphor screens. The screens were scanned on a Molecular Dynamics Typhoon PhosphorImager, and band intensities were quantified with ImageQuant 5.2. The data were fit using GraphPad Prism 6. All binding assays were performed in triplicate, and K_ds are reported as mean ± SEM. K_d values for phosphorylated dSLBP are estimates, because binding is tighter than can be measured by EMSA.

Crystallization. The preparation and crystallization of the hSLBP RBD-pT171:histone mRNA stem loop:3′hExo ternary complex followed previous protocols (18). To prepare dSLBP RPD:RNA complexes, dSLBP RPD-5E protein was mixed with a 28-nt histone mRNA stem loop (5′-GGCCAAAGGCCCUUUUCAGGGCCACCCA-3′; Dharmacon, Inc.) at a protein:RNA ratio of 1:1.2. The mixture was exchanged into a buffer containing 20 mM Hepes (pH 7.5) and 300 mM NaCl by dialysis overnight. The protein:RNA complex was purified using a Superdex-75 column and concentrated to 2 mg/mL dSLBP RPD-5E. Crystals of the protein:RNA complex were obtained by hanging-drop vapor diffusion by mixing 3 μL of the protein:RNA complex with 3 μL of a crystallization buffer containing 16% (wt/vol) PEG 3350, 0.2 M $Ca(Ac)_2$, 50 mM cacodylic acid, pH 6.5. The SeMet protein:RNA complex crystallized with the same crystallization buffer as native protein, but the space group differed (Table 1). Crystals of dSLBP RPD-WT:RNA complexes were obtained with a crystallization buffer containing 16% (wt/vol) PEG 1000, 0.2 M $Ca(Ac)_2$, 50 mM cacodylic acid, pH 6.5. All crystals were transferred stepwise to crystallization solution with 25% (vol/vol) ethylene glycol for cryoprotection and were flash-cooled in liquid nitrogen for data collection.

Data Collection and Structure Determination. X-ray diffraction data for the hSLBP RBD-pT171:histone mRNA stem loop:3′hExo ternary complex were collected at 100 K on beamline X-29A at the Brookhaven National Laboratory (wavelength 1.075 Å). The structure was refined with PHENIX (34), and manual model building was carried out with Coot (35). Ramachandran statistics were as follows: outliers, 0.0%; allowed, 2.8%; favored, 97.2% (36).

dSLBP X-ray diffraction data for native crystals were collected at 100 K on beamline BM-22 at the Advanced Photon Source (wavelength 1.000 Å), and anomalous data for SeMet crystals were collected at beamline ID-22 (wavelength 0.979 Å). Diffraction data were indexed and scaled with HKL2000 (37). The crystal structure was determined using single-wavelength anomalous diffraction data, and an initial dSLBP RPD-5E:histone mRNA stem-loop model was built using PHENIX (34). This initial model was used as a search model for molecular replacement (PHENIX AutoMR) with the dSLBP RPD-WT:RNA data. The structures were refined with PHENIX (34), and manual model building was carried out with Coot (35). Ramachandran statistics were as follows: dSLBP RPD-5E L245M/L253M (outliers, 0.0%; allowed, 9.3%; favored, 90.7%); dSLBP RPD-5E (outliers, 0.0%; allowed, 9.0%; favored, 91.0%); and dSLBP RPD-WT (outliers, 0.0%; allowed, 9.2%; favored, 90.8%) (36).

NMR Assignment Experiments. Free or histone mRNA stem-loop–bound ^{15}N-/^{13}C-labeled dSLBP RPD-5E was prepared as described above, except that *E. coli* cultures were grown in M9 medium containing appropriate isotopes. Data for backbone assignment experiments [HNCACB, CBCA(CO)NH, HNCA, and HNCO] were collected on a Varian Inova 600 MHz magnet installed with a cryo-probe. The assignment data were processed by NMRPipe (38) and analyzed by NMRViewJ (39). Because of the poor dispersion of the spectra, only partial assignment was accomplished for free dSLBP RPD-5E.

ITC. dSLBP RPD-5E, dSLBP RPD-EPNK, and histone mRNA stem loops were dialyzed at 4 °C overnight against 10 mM Hepes (pH 7.5), 100 mM NaCl in the same beaker to avoid subtle buffer differences. Protein concentrations were adjusted to 1 μM, and the RNA concentration was adjusted to 500 μM. Titration experiments were performed using a MicroCal iTC200 system at 4 °C. A single injection brought the RNA:protein molar ratio to 15:1. The experiments were performed in triplicate, and the heat-releasing peaks were integrated to calculate enthalpy changes. The dilution effect was measured by repeating the RNA injection with the same parameter settings in the absence of protein, and these values were subtracted from the experimental heat-releasing peaks.

Fluorescence Measurements. Protein samples for fluorescence measurements (dSLBP RPD-EPNK and -5E) were dialyzed into 20 mM Hepes (pH 7.5), 200 mM NaCl and diluted to 5 μM. Measurements were performed at 25 °C with a FluoroLog 3 spectrofluorometer (Horiba Scientific). To excite Tyr fluorescence and observe intrinsic FRET from the Tyr residues to Trp, the excitation wavelength was set to 270 nm, and fluorescence emission data were collected from 280–400 nm. Urea was added stepwise to 7.5 M. Blank spectra in the absence of protein at different urea concentrations were collected and subtracted from corresponding fluorescence spectra. Spectra were normalized to the Trp emission peak (around 355 nm) of W249. Peak intensities for Tyr residues (300 nm) at different urea concentrations were extracted to monitor Tyr–Trp FRET transfer efficiency.

Paramagnetic Relaxation Enhancement Experiments. To introduce an MTSL-labeling site, a Cys residue was added at the C terminus of dSLBP RPD-EPNK and dSLBP RPD-5E. The Cys-bearing proteins were purified with 1 mM TCEP added to all buffers. Immediately before MTSL labeling, TCEP was removed from the protein samples by passage through a Sephadex G-25 desalting column equilibrated in 20 mM Hepes (pH 7.5), 200 mM NaCl. MTSL was added in 15-fold excess and incubated overnight at 4 °C. Uncoupled MTSL was removed with a desalting column. To avoid potential intermolecular PRE, sample concentration was kept below 50 μM for paramagnetic spectrum collection. Diamagnetic spectra were collected by adding ascorbic acid to samples. The para- and diamagnetic spectra were processed with NMRPipe (38), and peak intensities were extracted with NMRViewJ (39).

Molecular Dynamics Simulations. Solution structures of the dSLBP RPD in free- and RNA-bound forms with T230 phosphorylation were generated using molecular dynamics. The initial structures were based on the RNA-bound structure of dSLBP RPD-5E. A phosphate group was introduced at T230, and two sets of parallel simulations were run with −1 and −2 oxidation states of the introduced phosphate group. The models were first energy-minimized in vacuum using the program Amber.12 (40), and then each optimized configuration was solvated in a box of water (13,766 water molecules in the RNA-free system and 23,876 water molecules in the RNA-bound system). Before equilibration, all systems were subjected to (*i*) a 1-ns belly dynamics run with fixed peptide (or peptide:RNA); (*ii*) minimization; (*iii*) low-temperature constant-pressure dynamics at fixed peptide (or peptide:RNA) to assure a reasonable starting density; (*iv*) minimization; (*v*) stepwise heating molecular dynamics at constant volume; and (*vi*) constant-volume molecular dynamics for 5 ns. All final unconstrained trajectories were calculated at 300 K under constant volume (30 ns; time step, 1 fs) using PMEMD (Amber.12) to accommodate long-range interactions (40). The parameters were taken from the FF12 force field for the protein (40) and the PARMBSC0 force field for the RNA (41). Phosphorylated Thr parameters were taken from the work of Homeyer, et al. (42).

In the X-ray crystal structures of dSLBP RPD, the C-terminal residues 256–276 were disordered. We used the program Rosetta3.4 (43) to obtain plausible models for these residues. The models were clustered, and 10 representative models for dSLBP RPD were selected based on the conclusion from PRE experiments that the C terminus may be located near residues S196, R197, and R198. The model structures were solvated in water and subjected to extensive molecular dynamics simulations of 100 ns using the above procedure with the Amber FF12 force field. Parallel sets of simulations were performed for singly phosphorylated dSLBP RPD-pTPNK and the fully phosphorylated dSLBP RPD (pTPNK motif and four C-terminal phospho-serine residues) with the phosphorylated Thr and Ser parameters taken from Homeyer, et al. (42). A representative trajectory from each system was used as the source for Movies S1 (pTPNK singly-phosphorylated) and S2 (fully phosphorylated), which were created with the program Chimera 1.7 (44).

Generalized order parameters (S^2) were calculated as described (45) using the formula $S^2 = \frac{1}{2}(3\sum_{i=1}^{3}\sum_{j=1}^{3}\langle\mu_i\mu_j\rangle^2 - 1)$, in which 1, 2, and 3 are the *x*, *y*, and *z* components, respectively, of the unit bond vector, N–H (where N is the amide nitrogen and H is the proton attached to it). In the case of proline, the C = O bond vector was used). The averaging of snapshots extracted every 50 ps was done for the last 60 ns of the simulations. Superposition of backbone heavy atoms of residues for the two simulations was carried out to remove the overall translation and rotation of the molecule.

ACKNOWLEDGMENTS. We thank X. C. Yang for expressing dSLBP and hSLBP in insect cells; J. Williams and the National Institute of Environmental Health Sciences (NIEHS) Protein Microcharacterization Facility for mass spectrometric analyses; L. Pedersen and the staff of the Southeast Regional Collaborative Access Team beamlines for assistance with X-ray data collection; R. Jackimowicz and H. Robinson for access to the X29A beamline at the National Synchrotron Light Source; the NIEHS NMR Group for advice and feedback regarding experimental design; and M. Sobhany for assistance with Isothermal Titration Calorimetry data collection. Fluorescence experiments were performed at the University of North Carolina Macromolecular Interactions Facility, and we thank A. Tripathy, Director of the facility, for his assistance. This work was supported in part by the Intramural Research Program of the National Institutes of Health (NIH), NIEHS (T.M.T.H.), and NIH Grants GM077175 (to L.T.), GM58921 (to W.F.M.), and GM29832 (to Z.D. and W.F.M.). E.F.D. is supported by the NIEHS, NIH, under Delivery Order HHSN273200700046U. The Advanced Photon Source used for this study was supported by the US Department of Energy, Office of Science, Office of Basic Energy Sciences, under Contract W-31-109-Eng-38.

1. Harris ME, et al. (1991) Regulation of histone mRNA in the unperturbed cell cycle: Evidence suggesting control at two posttranscriptional steps. *Mol Cell Biol* 11(5):2416–2424.
2. Marzluff WF, Wagner EJ, Duronio RJ (2008) Metabolism and regulation of canonical histone mRNAs: Life without a poly(A) tail. *Nat Rev Genet* 9(11):843–854.
3. Marzluff WF, Duronio RJ (2002) Histone mRNA expression: Multiple levels of cell cycle regulation and important developmental consequences. *Curr Opin Cell Biol* 14(6):692–699.
4. Dominski Z, Marzluff WF (1999) Formation of the 3′ end of histone mRNA. *Gene* 239(1):1–14.
5. Birnstiel ML, Busslinger M, Strub K (1985) Transcription termination and 3′ processing: The end is in site! *Cell* 41(2):349–359.
6. Martin F, Schaller A, Eglite S, Schümperli D, Müller B (1997) The gene for histone RNA hairpin binding protein is located on human chromosome 4 and encodes a novel type of RNA binding protein. *EMBO J* 16(4):769–778.
7. Mowry KL, Steitz JA (1987) Identification of the human U7 snRNP as one of several factors involved in the 3′ end maturation of histone premessenger RNA's. *Science* 238(4834):1682–1687.
8. Dominski Z, Yang XC, Marzluff WF (2005) The polyadenylation factor CPSF-73 is involved in histone-pre-mRNA processing. *Cell* 123(1):37–48.
9. Kolev NG, Yario TA, Benson E, Steitz JA (2008) Conserved motifs in both CPSF73 and CPSF100 are required to assemble the active endonuclease for histone mRNA 3′-end maturation. *EMBO Rep* 9(10):1013–1018.
10. Sabath I, et al. (2013) 3′-End processing of histone pre-mRNAs in Drosophila: U7 snRNP is associated with FLASH and polyadenylation factors. *RNA* 19(12):1726–1744.
11. Wagner EJ, et al. (2007) A genome-wide RNA interference screen reveals that variant histones are necessary for replication-dependent histone pre-mRNA processing. *Mol Cell* 28(4):692–699.

12. Streit A, Koning TW, Soldati D, Melin L, Schümperli D (1993) Variable effects of the conserved RNA hairpin element upon 3′ end processing of histone pre-mRNA in vitro. *Nucleic Acids Res* 21(7):1569–1575.
13. Dominski Z, Yang XC, Purdy M, Marzluff WF (2005) Differences and similarities between Drosophila and mammalian 3′ end processing of histone pre-mRNAs. *RNA* 11(12):1835–1847.
14. Thapar R, Marzluff WF, Redinbo MR (2004) Electrostatic contribution of serine phosphorylation to the Drosophila SLBP—histone mRNA complex. *Biochemistry* 43(29):9401–9412.
15. Dominski Z, et al. (2002) 3′ end processing of Drosophila melanogaster histone pre-mRNAs: Requirement for phosphorylated Drosophila stem-loop binding protein and coevolution of the histone pre-mRNA processing system. *Mol Cell Biol* 22(18): 6648–6660.
16. Borchers CH, et al. (2006) Combined top-down and bottom-up proteomics identifies a phosphorylation site in stem-loop-binding proteins that contributes to high-affinity RNA binding. *Proc Natl Acad Sci USA* 103(9):3094–3099.
17. Zhang M, Lam TT, Tonelli M, Marzluff WF, Thapar R (2012) Interaction of the histone mRNA hairpin with stem-loop binding protein (SLBP) and regulation of the SLBP-RNA complex by phosphorylation and proline isomerization. *Biochemistry* 51(15): 3215–3231.
18. Tan D, Marzluff WF, Dominski Z, Tong L (2013) Structure of histone mRNA stem-loop, human stem-loop binding protein, and 3′hExo ternary complex. *Science* 339(6117): 318–321.
19. Dominski Z, Erkmann JA, Greenland JA, Marzluff WF (2001) Mutations in the RNA binding domain of stem-loop binding protein define separable requirements for RNA binding and for histone pre-mRNA processing. *Mol Cell Biol* 21(6):2008–2017.
20. DeJong ES, Marzluff WF, Nikonowicz EP (2002) NMR structure and dynamics of the RNA-binding site for the histone mRNA stem-loop binding protein. *RNA* 8(1):83–96.
21. Zanier K, et al. (2002) Structure of the histone mRNA hairpin required for cell cycle regulation of histone gene expression. *RNA* 8(1):29–46.
22. Lakowicz JR (2006) *Principles of Fluorescence Spectroscopy* (Springer, New York), 3rd Ed, pp xxvi, 954 pp.
23. Clore GM, Iwahara J (2009) Theory, practice, and applications of paramagnetic relaxation enhancement for the characterization of transient low-population states of biological macromolecules and their complexes. *Chem Rev* 109(9):4108–4139.
24. Felitsky DJ, Lietzow MA, Dyson HJ, Wright PE (2008) Modeling transient collapsed states of an unfolded protein to provide insights into early folding events. *Proc Natl Acad Sci USA* 105(17):6278–6283.
25. Lipari G, Szabo A (1982) Model-free approach to the interpretation of nuclear magnetic resonance relaxation in macromolecules. 1. Theory and range of validity. *J Am Chem Soc* 104(17):4546–4559.
26. Whitfield ML, et al. (2000) Stem-loop binding protein, the protein that binds the 3′ end of histone mRNA, is cell cycle regulated by both translational and post-translational mechanisms. *Mol Cell Biol* 20(12):4188–4198.
27. Lanzotti DJ, Kaygun H, Yang X, Duronio RJ, Marzluff WF (2002) Developmental control of histone mRNA and dSLBP synthesis during Drosophila embryogenesis and the role of dSLBP in histone mRNA 3′ end processing in vivo. *Mol Cell Biol* 22(7):2267–2282.
28. Lanzotti DJ, et al. (2004) Drosophila stem-loop binding protein intracellular localization is mediated by phosphorylation and is required for cell cycle-regulated histone mRNA expression. *Mol Biol Cell* 15(3):1112–1123.
29. Williams AS, Marzluff WF (1995) The sequence of the stem and flanking sequences at the 3′ end of histone mRNA are critical determinants for the binding of the stem-loop binding protein. *Nucleic Acids Res* 23(4):654–662.
30. Wang ZF, Whitfield ML, Ingledue TC, 3rd, Dominski Z, Marzluff WF (1996) The protein that binds the 3′ end of histone mRNA: A novel RNA-binding protein required for histone pre-mRNA processing. *Genes Dev* 10(23):3028–3040.
31. Cho S, et al. (2011) Interaction between the RNA binding domains of Ser-Arg splicing factor 1 and U1-70K snRNP protein determines early spliceosome assembly. *Proc Natl Acad Sci USA* 108(20):8233–8238.
32. Xiang S, et al. (2013) Phosphorylation drives a dynamic switch in serine/arginine-rich proteins. *Structure* 21(12):2162–2174.
33. Dominski Z, Zheng LX, Sanchez R, Marzluff WF (1999) Stem-loop binding protein facilitates 3′-end formation by stabilizing U7 snRNP binding to histone pre-mRNA. *Mol Cell Biol* 19(5):3561–3570.
34. Adams PD, et al. (2010) PHENIX: A comprehensive Python-based system for macromolecular structure solution. *Acta Crystallogr D Biol Crystallogr* 66(Pt 2): 213–221.
35. Emsley P, Lohkamp B, Scott WG, Cowtan K (2010) Features and development of Coot. *Acta Crystallogr D Biol Crystallogr* 66(Pt 4):486–501.
36. Chen VB, et al. (2010) MolProbity: All-atom structure validation for macromolecular crystallography. *Acta Crystallogr D Biol Crystallogr* 66(Pt 1):12–21.
37. Otwinowski Z, Minor W (1997) Processing of X-ray diffraction data collected in oscillation mode. *Meth Enz* 276(Pt A):307–326.
38. Delaglio F, et al. (1995) NMRPipe: A multidimensional spectral processing system based on UNIX pipes. *J Biomol NMR* 6(3):277–293.
39. Johnson BA (2004) Using NMRView to visualize and analyze the NMR spectra of macromolecules. *Methods Mol Biol* 278:313–352.
40. Case DA, et al. (2012) AMBER 12. (University of California, San Francisco).
41. Pérez A, et al. (2007) Refinement of the AMBER force field for nucleic acids: Improving the description of alpha/gamma conformers. *Biophys J* 92(11):3817–3829.
42. Homeyer N, Horn AH, Lanig H, Sticht H (2006) AMBER force-field parameters for phosphorylated amino acids in different protonation states: Phosphoserine, phosphothreonine, phosphotyrosine, and phosphohistidine. *J Mol Model* 12(3):281–289.
43. Leaver-Fay A, et al. (2011) ROSETTA3: An object-oriented software suite for the simulation and design of macromolecules. *Methods Enzymol* 487:545–574.
44. Pettersen EF, et al. (2004) UCSF Chimera—a visualization system for exploratory research and analysis. *J Comput Chem* 25(13):1605–1612.
45. Trbovic N, et al. (2009) Protein side-chain dynamics and residual conformational entropy. *J Am Chem Soc* 131(2):615–622.